Volcanic cloud detection using Sentinel-3 satellite data by means of neural networks: the Raikoke 2019 eruption test case

Ilaria Petracca[1], Davide De Santis[1], Matteo Picchiani[2,3], Stefano Corradini[4], Lorenzo Guerrieri[4], Fred Prata[5], Luca Merucci[4], Dario Stelitano[4], Fabio Del Frate[1], Giorgia Salvucci[1] and Giovanni Schiavon[1]

[1] Department of Civil Engineering and Computer Science Engineering, Tor Vergata University of Rome, 00133, Italy
[2] GEO-K s.r.l., Rome, Italy
[3] GMATICS s.r.l., Rome, Italy
[4] Istituto Nazionale di Geofisica e Vulcanologia, ONT, 00143 Rome, Italy
[5] AIRES Pty Ltd., Australia

Correspondence to: Ilaria Petracca (ilaria.petracca@uniroma2.it)

Abstract

The accurate automatic volcanic cloud detection by means of satellite data is a challenging task and of great concern for both scientific community and stakeholder due to the well-known issues generated by a strong eruption event in relation to aviation safety and health impact. In this context, machine learning techniques applied to recent spaceborne sensors acquired data have shown promising results in the last years.

This work focuses on the application of a neural network based model to Sentinel-3 SLSTR (Sea and Land Surface Temperature Radiometer) daytime products in order to detect volcanic ash plumes generated by the 2019 Raikoke eruption. The classification of the clouds and of the other surfaces composing the scene is also carried out. The neural network has been trained with MODIS (MODerate resolution Imaging Spectroradiometer) daytime imagery collected during the 2010 Eyjafjallajökull eruption. The similar acquisition channels of SLSTR and MODIS sensors and the events comparable latitudes foster the robustness of the approach, which allows overcoming the lack in SLSTR products collected in previous mid-high latitude eruptions. The results show that the neural network model is able to detect volcanic ash with good accuracy if compared with RGB visual inspection and BTD (Brightness Temperature Difference) procedure. Moreover, the comparison between the ash cloud obtained by neural network and a plume mask manually generated for the specific SLSTR considered images, shows significant agreement. Thus, the proposed approach allows an automatic image classification during eruption events, which it is also considerably faster than time-consuming manually algorithms (e.g. find the best BTD product-specific threshold). Furthermore, the whole image classification indicates an overall reliability of the algorithm, in particular for meteo-clouds recognition and discrimination from volcanic clouds.

Finally, the results show that the NN developed for the SLSTR nadir view is able to properly classify also the SLSTR oblique view images.

1 Introduction

In general, from the start of the eruption, the volcanic emission is composed by both coarse and fine particles. The coarser fall down to the volcanic edifice, while the finer are transported by the wind. The solid part of the volcanic plume is basically composed by ash particles while the gaseous part is made mainly of water vapour (H_2O), carbon dioxide (CO_2) and sulphur dioxide (SO_2) gases (Oppenheimer et al., 2011; Shinohara et al., 2008). Depending on the eruptive intensity, the volcanic cloud can reach different altitudes in the atmosphere thus affecting environment (Delmelle et al.,2002; Craig et al., 2016) , climate (Haywood et al., 2000; Solomon et al., 2011; Bourassa et al., 2012), human health (Delmelle et al.,2002; Mather et al., 2003; Horwell et al., 2006; 2013) and aircraft safety (Casadevall et al., 1994; Zenher 2010).

The detection procedure consists in identifying the presence of certain species in the atmosphere and discriminating them against other species. Thus, volcanic ash detection is related to the discrimination of the areas (pixels in an image), which are affected by the presence of these particles. First evidences about the possibility to detect the volcanic cloud by means of remote sensing data arise in the eighties (Prata, 1989a,b). The method used for the detection problem of volcanic ash particles lies in the ability to discriminate between volcanic clouds and meteorological ice and water vapour clouds by exploiting the different spectral absorption in the Thermal InfraRed (TIR) spectral range. In this interval the absorption of ash particles with radius between 0.5 µm and 15 µm at wavelength of 11 µm is larger than the absorption of ash particles at 12 µm. The opposite happens for weather clouds, which absorb more significantly at longer TIR wavelengths. Therefore, the Brightness Temperature Difference (BTD), i.e. the difference between the Brightness Temperatures (BTs) at 11 and 12 microns, turns out to be negative ($\Delta T11\mu m\text{-}12\mu m < 0$ °C) for region affected by volcanic clouds and positive ($\Delta T11\mu m\text{-}12\mu m > 0$ °C) for region affected by meteorological clouds.

The BTD approach is the most used method for the volcanic cloud identification. It is effective and simple to be applied, even if it can lead to false alarms in some cases: over clear surfaces during night, on soils containing large amounts of quartz (such as deserts), on very cold or ice surfaces, in presence of high water vapour content (Prata et al., 2001a). As already mentioned, the discrimination between volcanic and weather clouds is a challenging task, since the region of the overlap of the two objects shows a mixed behaviour not easily recognizable. In these mixed scenarios, the BTD can be negative not only for volcanic clouds but also for meteorological clouds; thus, some false positive results may occur, as the case of high weather clouds. False negative results may arise in the case of high atmospheric water vapour content: the water vapour contribution can hide and cancel out the ash particles effects on the BTD, and then the ashy pixels cannot be revealed. In these cases a correction procedure can be applied (Prata et al., 2001b; Corradini et al., 2008; 2009). Among the procedures described, other algorithms, based on the use of different spectral channels, have been developed (Francis et al., 2012; Pavolonis et al., 2010a,b).

For these reasons, it seems appropriate to use advanced classification schemes to address the task of the ash detection, such as approaches which make use of machine learning techniques, avoiding to find for each product the best BTD threshold for creating the volcanic cloud mask manually, which can be a considerable time-consuming process.

64 For aerosol and cloud detection, a neural network (NN) (Bishop et al., 1994; Atkinson et al., 1997; Di Noia and Hasekamp,
65 2018) based algorithm allows solution of a classification problem. Starting from inputs containing spectral radiance values
66 acquired in specific wavelength, the model generates a prediction in output by assigning to each pixel of the original image a
67 predefined class. In previous research, neural networks have already shown significant effectiveness in terms of atmospheric
68 parameter extraction (Gardner et al., 1998; Picchiani et al., 2011; Sellitto et al., 2012; Di Noia et al., 2013; Picchiani et al.,
69 2014; Piscini et al., 2014). A strong advantage of using a NN based approach for volcanic cloud detection is that once the
70 model is trained on a statistical representative selection of test cases, new imagery acquired over new eruptions can be
71 accurately (depending on the training phase) classified in near real time allowing significant improvements in critical situations
72 and in emergency management.
73 In this work, we developed a NN based algorithm for volcanic cloud detection using Sentinel-3 SLSTR (Sea and Land Surface
74 Temperature Radiometer) daytime data with a model trained on MODIS (MODerate resolution Imaging Spectroradiometer)
75 daytime images. This is possible since the two sensors have similar spectral bands and it represents an advantage as there are
76 currently limited amounts of SLSTR products available for eruptive events. The use of MODIS as a proxy for SLSTR was
77 already successfully tested in a previous work investigating the complex challenge of distinguishing ice and weather clouds
78 (also containing ice) using neural networks on SLSTR data (Picchiani et al., 2018). As test case, the Raikoke 2019 eruption
79 has been considered in this work.

2 Case study: the Raikoke 2019 eruption

81 The Raikoke volcano is located in the Kuril Island chain, near the Kamchatka Peninsula in Russia (48.3° N, 153.2° E). On
82 June 21, 2019 at about 18:00 UTC Raikoke started erupting and continued erupting until about 03:00 UTC on 22 June 2019).
83 During this period, Raikoke released large amount of ash and SO_2 into the stratosphere.
84 Figure 1 shows a time-series of 11 µm brightness temperatures (BTs) determined from the Himawari-8 AHI sensor at 10-
85 minute intervals for the first 18 hrs of the eruption. With the purpose of searching for high (cold) clouds associated with a
86 vertically ascending clouds due to an eruption, and not of meteorological origin, discrete eruptions were identified by
87 comparing AHI BTs near the vent with those some distance upwind from the vent. The Himawari-8 time-series shows a
88 sequence of eruptions (12 in all) and a sustained period of activity between 22:40 of 21 June and 02:10 of 22 June, when the
89 majority of ash and gas was emitted. The estimated time of an eruption event was determined by examining animated images
90 and consequently the times of eruptions shown do not always coincide with the coldest cloud-top.
91 It is estimated from the AHI data that June 2019 Raikoke eruption produced approximately 0.4–1.8 Tg of ash and 1–2 Tg of
92 SO_2 (Prata, private communication). The amount of water vapour emitted is unknown, but would have been considerable.
93 These emissions would have led to copious amounts of water and ice clouds being produced, making the composition of the
94 transported clouds both complex and changing with time.
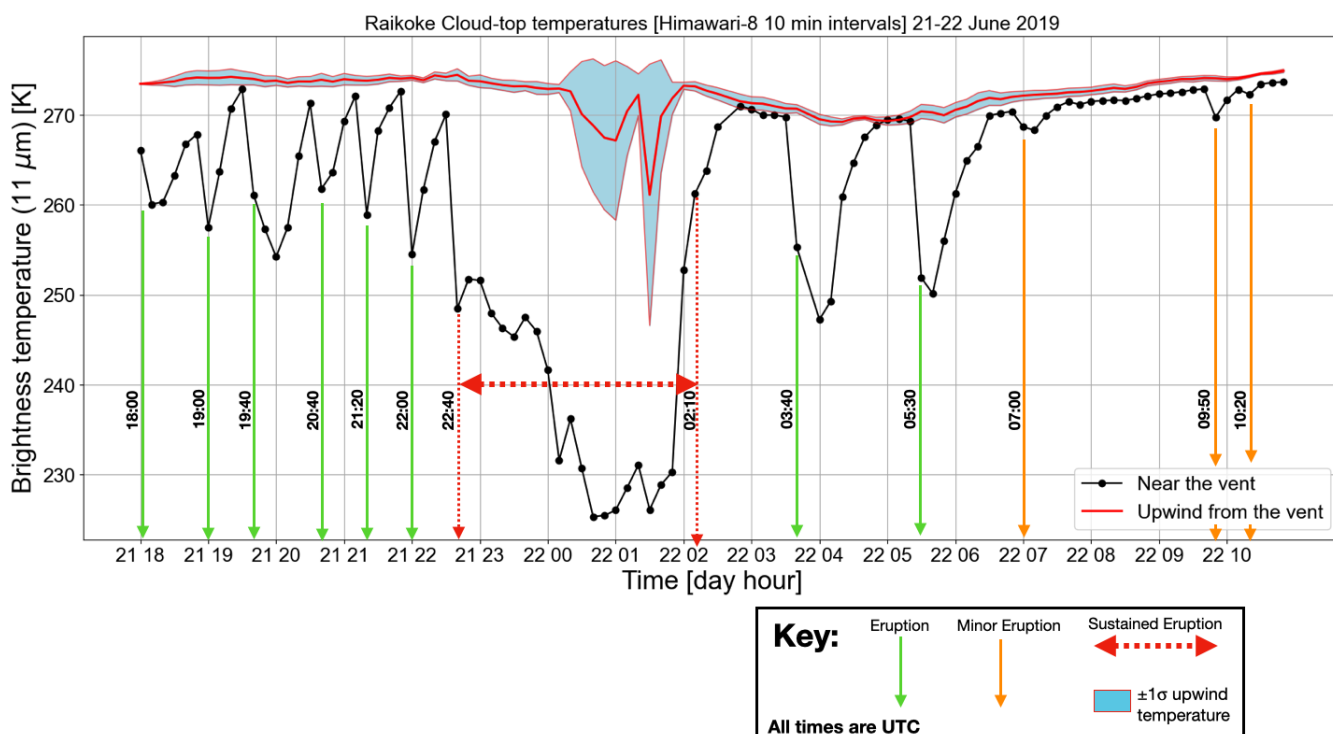
Figure 1: Time-series of eruptions from Raikoke during the first 18 hrs of activity. The times of eruptions was estimated from the imagery and does not always coincide with the coldest cloud tops.

3 Methodology

A multilayer perceptron neural network (MLP NN) was trained with MODIS daytime data and then it was applied to Sentinel-3/SLSTR daytime products, in order to discriminate ashy pixels from others, following the scheme reported in Figure 2.

The output of the proposed model is the SLSTR image fully classified in eight different surfaces: ash over sea, ash over cloud, ash over land, sea, land and ice surfaces, water vapour clouds and ice clouds. This approach has been used because of the long available time series of MODIS data, the quality of MODIS products (Picchiani et al., 2011; 2014; Piscini et al., 2014) and the spatial/spectral similarities between MODIS and SLSTR (see Table 1).

MODIS aboard the NASA-Terra/Aqua polar orbit satellites is a multispectral instrument, with 36 channels from VIS to TIR, a spatial resolution from 0.25 to 1 km, and a revisit time of 1–2 days. SLSTR is a dual view scanning radiometer, with 9 channels on board of Sentinel-3A and Sentinel-3B. The pixel size ranges from 500x500 m for VNIR and SWIR bands to 1x1 km for TIR bands. The feasibility of this procedure has also been confirmed for high latitudes (Picchiani et al., 2018), since our study area is located in medium-high latitudes.

112 **Table 1:** Correspondence between MODIS and SLSTR channels.

SLSTR Channel	λ Centre (µm)	MODIS Channel	Bandwidth (µm)
S1	0.555	4	0.545-0.565
S2	0.659	1	0.620-0.670
S3	0.865	2	0.862-0.877
S4	1.375	26	1.360-1.390
S5	1.61	6	1.628-1.652
S6	2.25	7	2.105-2.155
S7	3.74	20	3.660-3.840
S8	10.85	31	10.780-11.280
S9	12	32	11.770-12.270

113
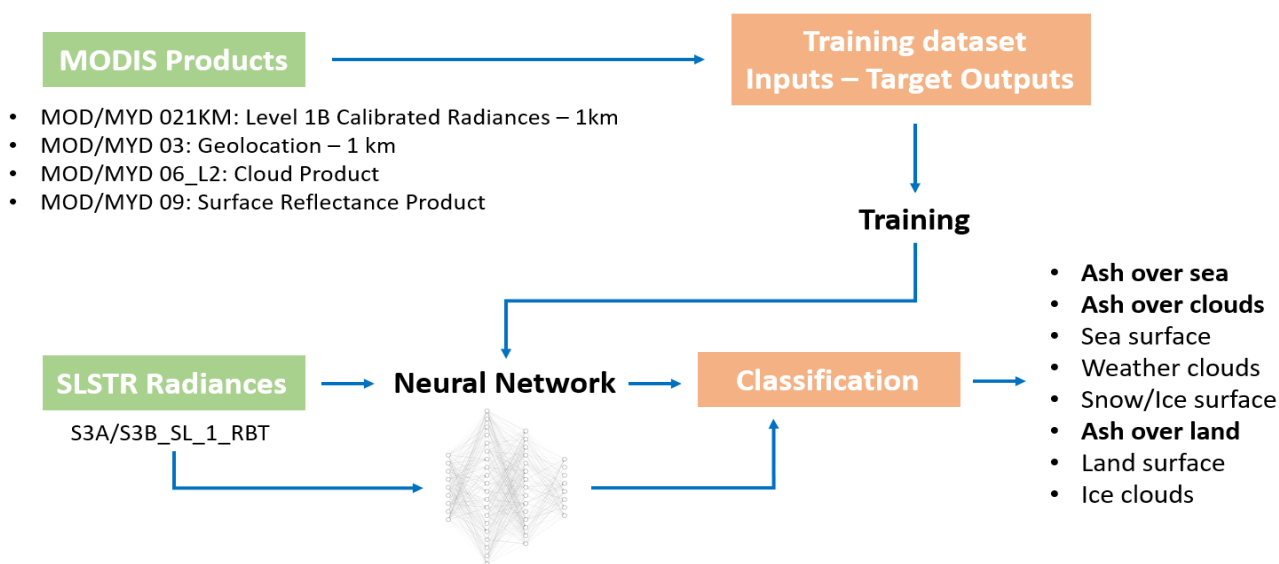
114

115 **Figure 2:** Overall diagram of the followed procedure for the classification process with NN model.

116 The training set consists of nine MODIS data acquired over the Eyjafjallajokull volcano area during the 2010 eruption (from

117 May 6th to May 13th), for a total of about 5400 patterns for each class available for the training of the model. The total number

118 of patterns has been divided into three subsets: 75% training set, 20% validation set, 5% test set. A neural network with two

119 hidden layers was trained and then it was applied to four Sentinel-3 SLSTR RBT (Radiance and Brightness Temperature)

120 (SL_1_RBT) images collected during the Raikoke 2019 eruption. Table 2 shows the details of MODIS and SLSTR data used

121 for this work.

122

123 **Table 2:** Training set (MODIS) from the Eyjafjallajökull 2010 eruption; Sentinel-3 Raikoke 2019 classified products.

Date	Time UTC	Platform	Training/Application
6 May 2010 (JD 126)	11:55	Terra	Training
9 May 2010 (JD 129)	12:25	Terra	Training
11 May 2010 (JD 131)	12:10	Terra	Training
11 May 2010 (JD 131)	12:15	Terra	Training
11 May 2010 (JD 131)	13:50	Terra	Training
11 May 2010 (JD 131)	14:05	Aqua	Training
12 May 2010 (JD 132)	12:55	Terra	Training
13 May 2010 (JD 133)	12:00	Terra	Training
13 May 2010 (JD 133)	13:40	Terra	Training
22 June 2019 (JD 173)	00:07	Sentinel-3A	Application
22 June 2019 (JD 173)	23:01	Sentinel-3B	Application

124

125 In order to build the NN training patterns, a semi-automatic procedure, that exploits MODIS radiances and standard products,

126 has been developed. The MODIS products considered for the extraction of the training patterns are the following:

127   ●   MOD/MYD 021KM, Level 1B Calibrated Radiances – 1 km, which gives the radiance values for each MODIS band;

128   ●   MOD/MYD 03, Geolocation – 1 km, used for the Land/Sea Mask;

129   ●   MOD/MYD 06_L2, Cloud Product, containing cloud parameters, used for the Cloud Mask*;*

130   ●   MOD/MYD 09, Surface Reflectance Product, containing an estimate of the surface spectral reflectance measured at

131   ground level; it is used for the Ice Mask;

132 where "MOD" and "MYD" stands for MODIS-Terra and MODIS-Aqua products respectively.

133 The semi-automatic procedure for the extraction of training patterns starting from MODIS data, basically consists in using

134 MODIS products to create binary "masks" identifying the different objects/surfaces, and then replace them by "classes",

135 consisting of matrices containing radiance values ($W/(m^2 sr \mu m)$) extracted from the MODIS product MOD/MYD021KM. In

136 this way each object is radiometrically characterized. The identification of the ashy pixel is pursued by creating a mask

137 according to specific BTD thresholds (from 0.0 to -0.4 °C) and a manual correction performed through visual inspection of

138 each MODIS image. The other objects are identified using both MODIS bands and MODIS standard products. Once each

139 object/surface has been defined, they are associated with the corresponding class. Then a set of input-output samples for the

140 training phase is generated, where the input consists of the set of radiances measured for the given pixel and the output is a

141 binary vector with value 1 associated with the corresponding class and value 0 for the other classes.

142 Table 3 shows the classification map legend for each classified product presented in this work, in which eight classes are

143 discriminated, each one representing a surface/object.

144

145 **Table 3:** Classification map legend.

Class ID	Surface/Object	Name	Colour
1	Ash over sea	*Ash_sea*	■
2	Ash over clouds	*Ash_cloud*	■
3	Sea surface	*Sea*	■
4	Weather clouds	*Cloud*	■
5	Snow/Ice surface	*Ice*	
6	Ash over land	*Ash_land*	■
7	Land surface	*Land*	■
8	Ice clouds	*Cloud_ice*	■
-	Masked out pixels	*Not classified*	■

146
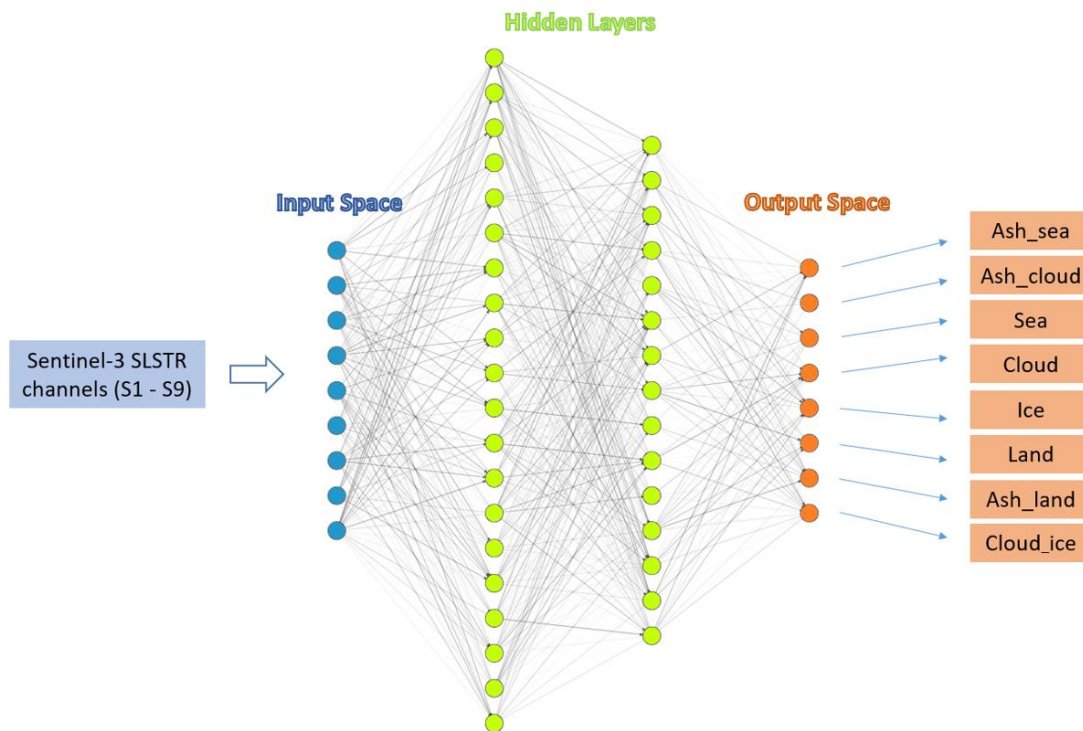
147

148 **Figure 3:** NN topology for ash detection.

149 The NN final model consists of nine inputs, which are the radiances in the SLSTR selected channels, while the output space

150 is composed of eight classes, which are the objects/surfaces which the net has to classify. After doing several tests the optimum

151 topology of the NN turns out to be the combination of two hidden layers with 20 and 15 neurons respectively. The final neural

152 network architecture used for ash detection in this work is shown in Figure 3. The proposed algorithm includes a post

153 processing operation in order to avoid false positive results for land and sea classes. This a posteriori filter is applied both to

154 the resulting NN land and sea classes. It allows masking out the pixels which the NN classifies as land/sea which do not belong

155 to the Sentinel-3/SLSTR land/sea mask standard product, which is always available and thus it can be used to increase the

156 precision of the algorithm. The filtered out pixels have been inserted in a class named "not classified", as reported in Table 3.

157 For classification problems approached with machine learning algorithms, one of the most used accuracy metrics for the

158 performance evaluation is the confusion matrix, where each predicted output class is compared to the corresponding ground

159 truth considered in the validation dataset. An overall accuracy of 90.9% was obtained at the end of the NN training phase for

160 the proposed neural network model (see Figure 4).

161
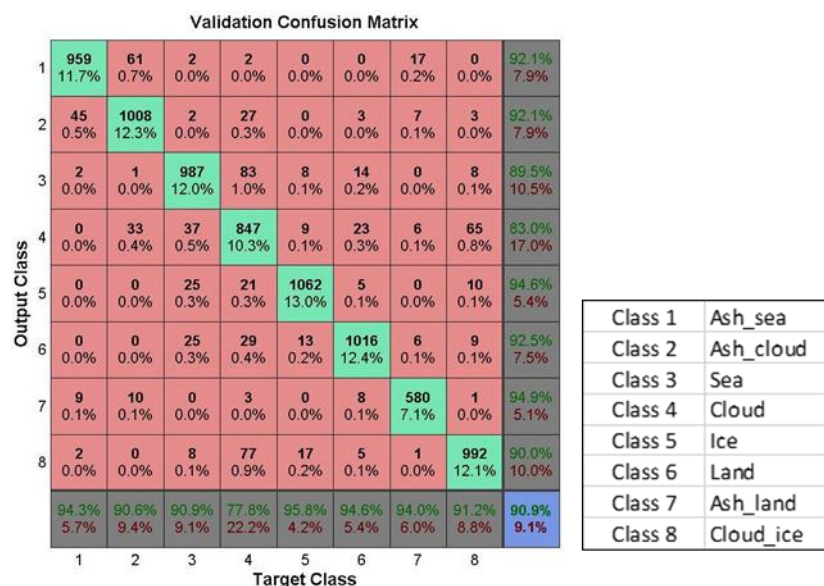
162

163 **Figure 4:** Confusion matrix on validation set.

164 The target class represents the "ground truth" of each class, while the output class refers to the prediction of the NN. The

165 diagonal shows that most of the total of the pixels have been correctly classified (green boxes). The number of pixels incorrectly

166 classified are placed out of the diagonal. Commission and omission errors are reported in the last grey column and row

167 respectively.

168 The MODIS products used for training the model were acquired in nadir view only. The trained network was applied to SLSTR

169 products acquired both in nadir and oblique view.

4 Results and Discussion

The neural network algorithm previously described was applied to Sentinel-3/SLSTR daytime images acquired on Raikoke during the 2019 eruption. The Sentinel-3A/SLSTR and Sentinel-3B/SLSTR products collected the 22 June 2019 at 00:07 and 23:01 UTC have been considered (see Table 2).
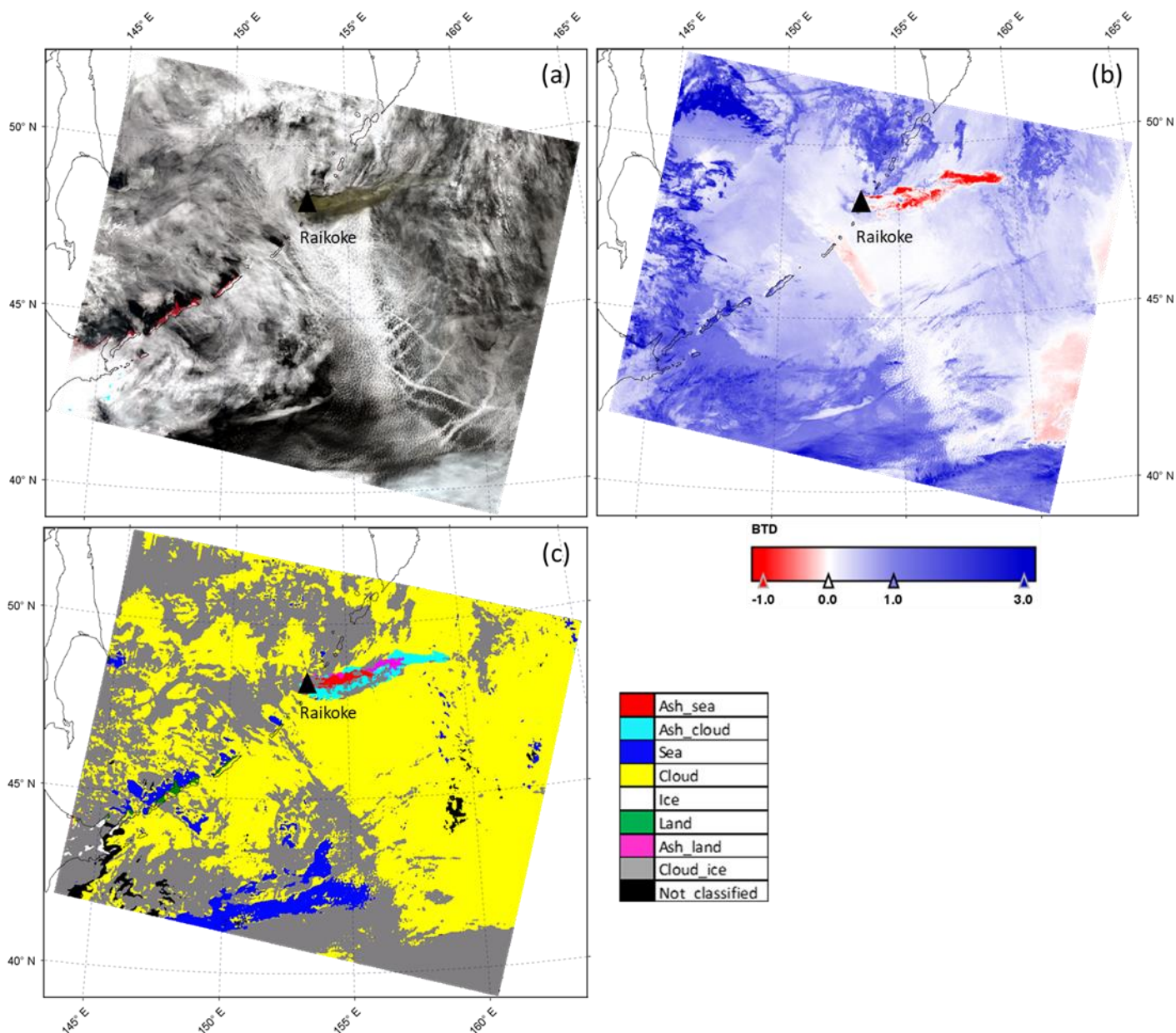
Figure 5: Sentinel-3A/SLSTR image collected on Raikoke the 22 Jun 2019 at 00:07 UTC, nadir view. (a) RGB; (b): BTD; (c): NN classification.

Figure 5(a) shows the RGB colour composite of the S3A/SLSTR image acquired on Raikoke the 22 June 2019 at 00:07 UTC. The RGB composite has been carried out by considering the SLSTR visible (VIS) channels S3 (868 nm), S2 (659 nm) and S1 (554 nm) for R, G and B, respectively. In Figure 5(b) the BTD map is displayed, where red and blue pixels represent negative and positive BTD respectively. The BTD is computed by making the difference between the brightness temperature of the SLSTR thermal infrared channels S8 and S9 centred at 10.8 and 12 μm. The output of the NN classification is shown in Figure 5(c) with the corresponding colour legend, where each colour represents the classified surface/object.
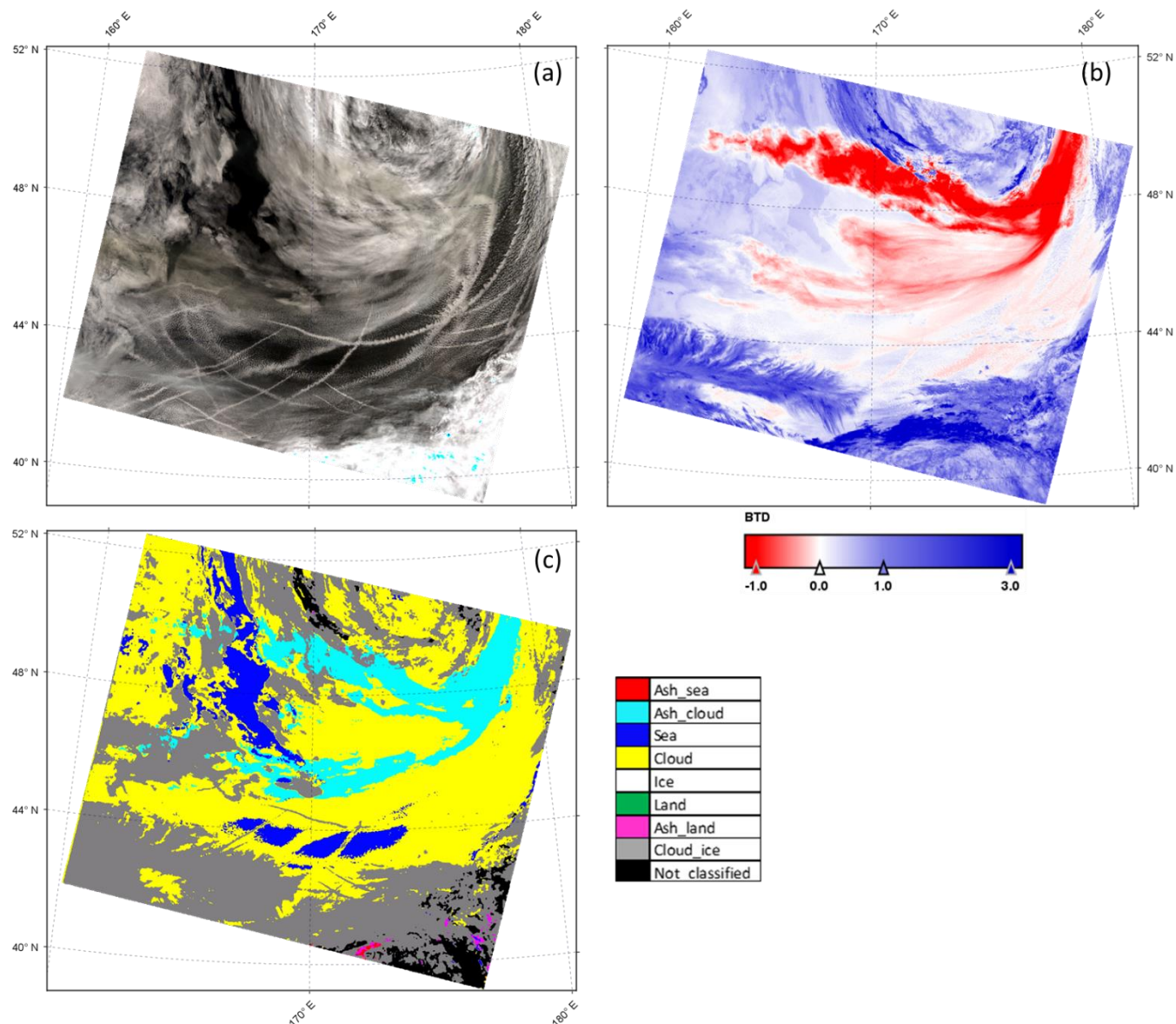
Figure 6: Sentinel-3B/SLSTR image collected on Raikoke the 22 June 2019 at 23:01 UTC, nadir view. (a): RGB; (b): BTD; (c): NN classification.

186 As Figure 5(a) shows, the RGB composite emphasizes the presence of a wide distribution of meteorological clouds and a

187 significant signal derived from the volcanic cloud (brown pixels). The BTD (Figure 5(b)), obtained with a threshold of 0 °C,

188 shows the presence of the volcanic cloud together with a significant number of false negative (volcanic cloud pixels not

189 identified near the vents) and false positive (pixels identified as volcanic cloud but that are not below the volcanic cloud and

190 along the right edge of the scene) pixels.

191 Despite the challenging scenario, the NN algorithm shows its ability to detect the volcanic cloud and to classify the whole

192 image, by detecting with good accuracy meteorological clouds composed of water droplets (yellow) and ice (grey), sea (blue)

193 and land (green) surfaces, and volcanic ash clouds, as reported in Figure 5(c). Looking at the cloud masks generated with the

194 NN algorithm (yellow and grey) and by comparing them with the RGB natural colour composite of the SLSTR product, a high

195 agreement in terms of spatial features can been observed. From the comparison between NN output classes and RGB composite

196 we can observe that also land (green) and sea (blue) pixels are properly detected in the area where they actually lie.

197 From a qualitative comparison between the NN plume mask and the RGB composite, we can state that the NN correctly

198 identifies the volcanic cloud class in the area where it seems actually present, even if some pixels are misclassified as ash-on-

199 land (magenta pixels). As Figure 5 shows, the NN algorithm is able to detect a wide volcanic cloud area and much less false

200 positives compared to the BTD approach. In particular the difference found near the vents can be due to the complete opacity

201 of the cloud. Here the ash cloud optical thickness is so high that the BTD is null.

202 Following the same visualization scheme of Figure 5, the results derived from the application of the trained NN model to the

203 S3B/SLSTR image acquired the 22 June 2019 at 23:01 UTC are reported in Figure 6. In this second image, all the ashy pixels

204 are classified by the NN model as ash above meteorological clouds (cyan pixels). This seems reasonable being the scenario

205 mostly dominated by weather clouds, as we can also observe looking at the NN classification, which assigns the majority of

206 the pixels to the water vapour cloud class (yellow) and to the ice cloud class (grey). The NN classification shows also the

207 presence of sea pixels (blue), which are located in the same area identifiable using the RGB composite. In this case, from the

208 RGB composite (Figure 6(a)), unlike to what can be seen in the midnight image, it is not straightforward to identify the volcanic

209 plume by visual inspection. Indeed, this image was collected about 24 hours later than the previous one and thus the plume

210 has been transported through the atmosphere and dispersed. A qualitative comparison between the NN classification (Figure

211 6(c)) and the BTD map (Figure 6(b)) shows considerable differences between the two methods. The BTD, obtained with a

212 threshold of 0 °C, identifies a wider area (red pixels) affected by the volcanic cloud respect to the NN ash mask (cyan pixels).

213 We can notice that the BTD map includes some aerial trails (recognizable by the shape in the RGB composite) in the ash mask,

214 which represent of course false positive results.

215 Figure 7 shows the RGB composite and the NN classification for the SLSTR oblique view product collected the 22 June 2019

216 at 00.07 UTC (Figure 7(a) and Figure 7(b)) and 23.01 UTC (Figure 7(c) and Figure 7(d)) respectively.

217 Looking at results obtained for the oblique view (Figure 7), we can observe that for the S3B/SLSTR image collected the 22

218 June 2019 at 23.01 UTC the NN model produces good results, which are also in accordance to the NN output obtained for the

219   processing of nadir view image acquired at the same time. For the S3A/SLSTR image collected the 22 June 2019 at 00.07

220   UTC, the NN results are instead less accurate; this is due to the opacity of the volcanic cloud.
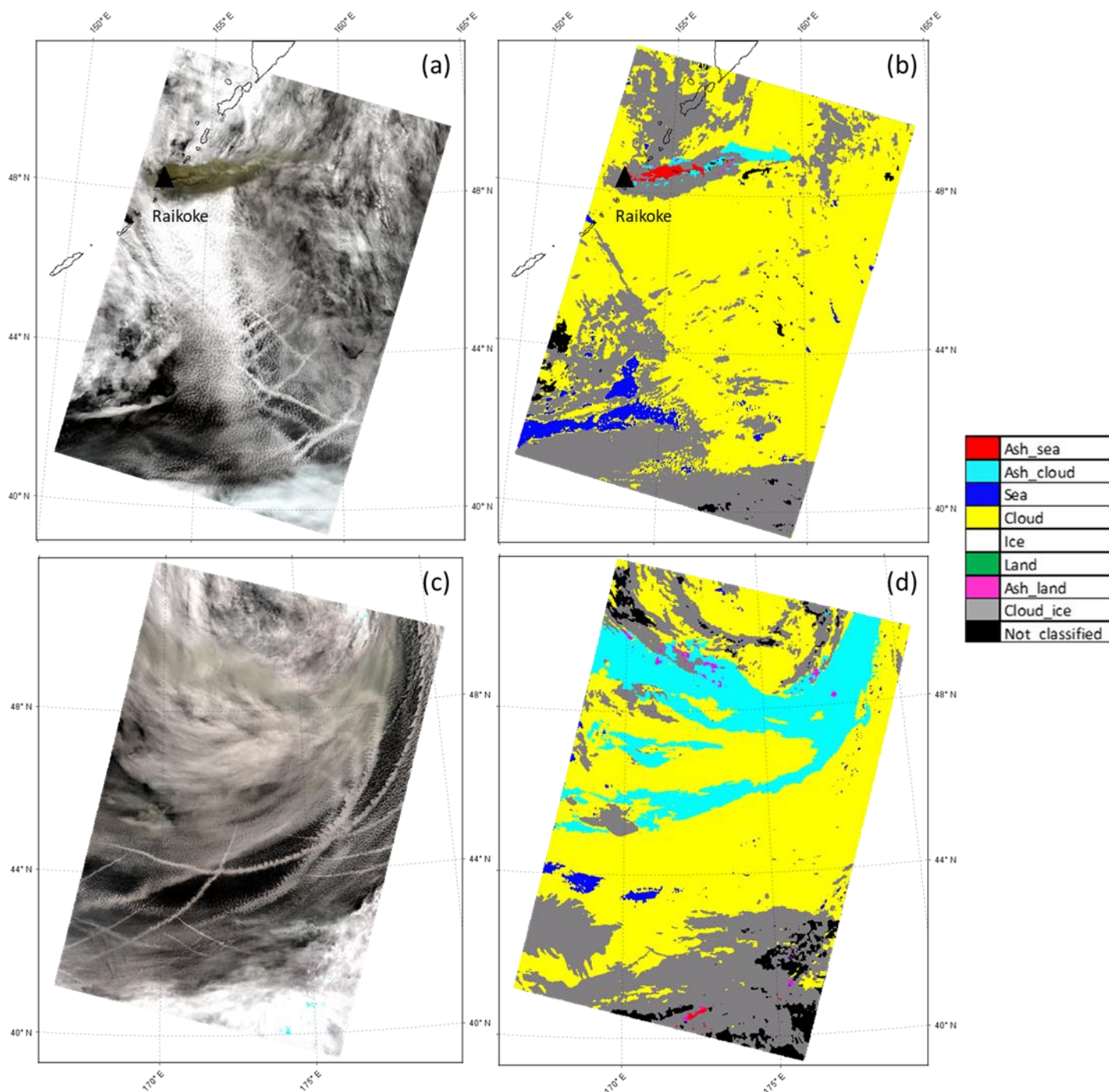
221

222   **Figure 7:** Sentinel-3A/SLSTR image collected on Raikoke the 22 Jun 2019 at 00:07 UTC, oblique view ((a) and (b)); Sentinel-3B/SLSTR

223   image collected on Raikoke the 22 June 2019 at 23:01 UTC, oblique view ((c) and (d)). (a) and (c): RGB; (b) and (d): NN classification.

224 A significant point to be discussed is that the results obtained in this work highlighted the robustness and transferability for a
225 NN model learning from one single event in a specific location in the world with specific background condition (latitude,
226 longitude, geometry of acquisition, atmospheric condition, season, etc) and successfully operating in a different scenario.

4.1 Validation

228 The capability of the NN to correctly detect pixels containing ash was validated by making a pixel per pixel comparison with
229 a reference plume mask generated manually (hereafter MPM) in order to obtain the best accurate *ground truth* as possible in
230 each SLSTR product. For the image collected at 00:07 UTC the MPM creation was performed selecting a region around the
231 volcanic cloud (clearly recognizable as it is at the beginning of the eruption) and then considering only the pixels with 11 µm
232 brightness temperature < 270 K. In this case the BTD alone it is not very useful as the high value of the ash optical thickness
233 of the cloud (especially close to the vent) produces many pixels with BTD values near zero, not distinguishable from adjacent
234 pixels characterized by meteorological clouds. For the image collected at 23:01 UTC, the identification of the volcanic cloud
235 is much more difficult due to its larger spread and dilution; in this case the MPM was obtained considering the pixels with
236 BTD < -0.25 °C, even if probably this choice implies that some ashy pixels were discarded. On the other hand, using an higher
237 BTD threshold will produce a lot of false positive pixels. In general, the creation of an accurate manual plume mask is time
238 consuming and case-sensitive and often requires the presence of an operator; so the generation of a volcanic cloud mask with
239 a fast, automatic and case-independent procedure would be a rather significant improvement.

240 Because the MPM doesn't distinguish between the different surfaces under the ash cloud, the validation is performed by
241 considering the total of the ashy pixels detected from the NN (i.e. the sum between *ash_land*, *ash_sea* and *ash_cloud*).

242 Figure 8 shows the MPM, created as described above, and the comparison between NN plume mask (hereafter NNPM) and
243 MPM for S3A/SLSTR image collected on Raikoke the 22 June 2019 at 00:07 UTC (Figure 8(a) and Figure 8(b)) and
244 S3B/SLSTR image collected on Raikoke the 22 June 2019 at 23:01 UTC (Figure 8(c) and Figure 8(d)).

245 In relation to the images which display the comparison between NN output and MPM (Figure 8(b) and Figure 8(d)), green
246 areas indicate the pixels for which both the MPM and NN ash masks detect the presence of volcanic cloud, red pixels represent
247 the areas classified as ash only by the MPM; blue ones are the pixels classified as ash only according to the NN model. We
248 can observe that most of the volcanic cloud is displayed in green for both products (00.07 UTC and 23.01 UTC), indicating
249 good matching between the two approaches. This is also confirmed by the scores in Table 4, which shows the number of pixels
250 classified as ash by both NN and MPM (green pixels), the number of pixels classified as ash only by NN (blue pixels), the
251 number of pixels classified as ash only by MPM (red pixels). We can observe that the two approaches are in accordance for
252 the majority of the pixels, albeit they differ in discriminating volcanic cloud in some regions.

253

Table 4: Comparison between the NN plume mask (NNPM) and the manual plume mask (MPM) for each SLSTR classified product (pixels number for each class). The total number of classified pixels is 1614405 for the S3A/SLSTR at 00.07 UTC image and 1701319 for the S3B/SLSTR at 23.01 UTC image respectively.

Product Classified Product	NNPM and MPM	Only NNPM	Only MPM
S3A/SLSTR at 00.07 UTC	13545	5568	6275
S3B/SLSTR at 23.01 UTC	136435	39991	71223
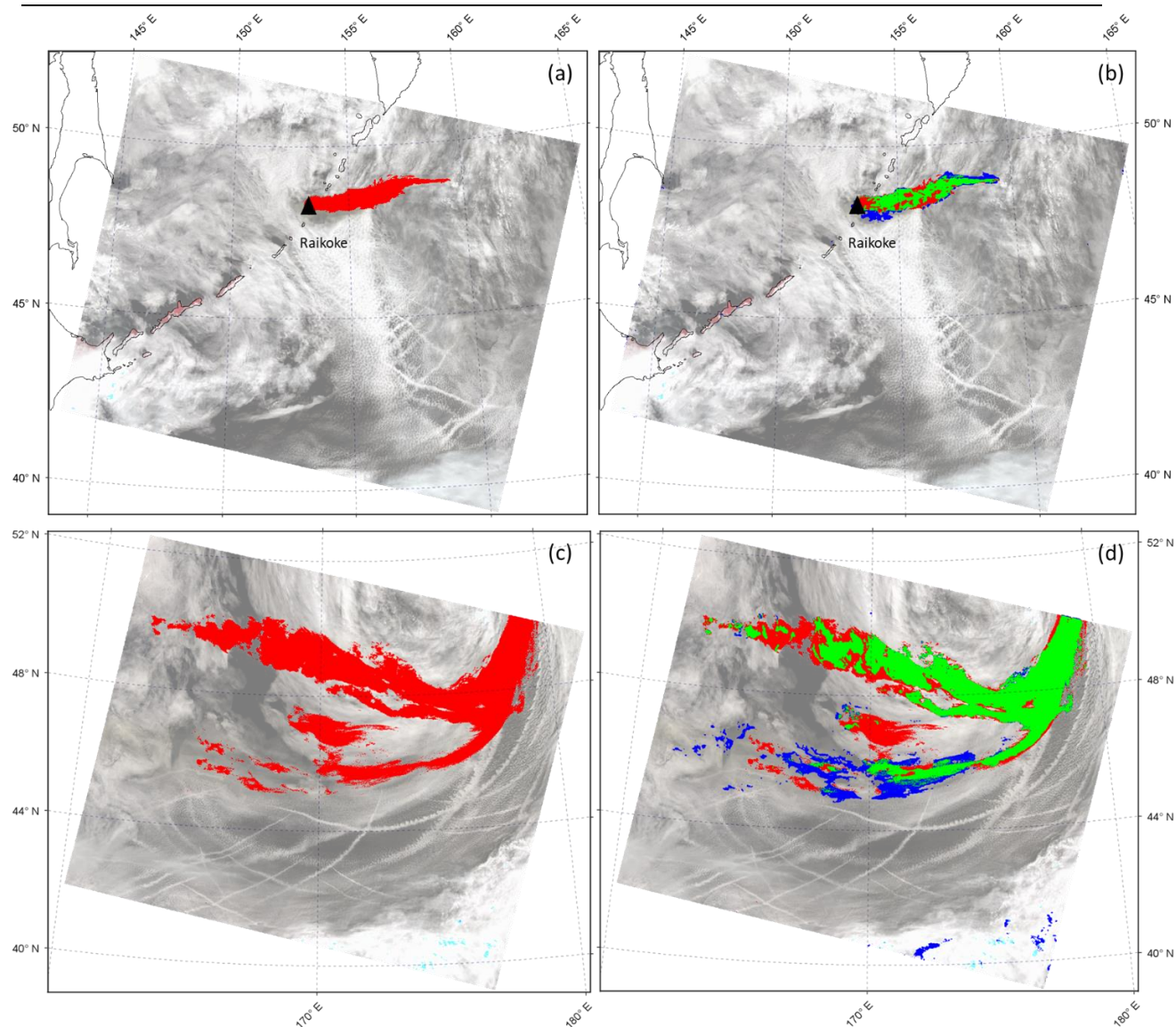
Figure 8: Sentinel-3A/SLSTR image collected on Raikoke the 22 June 2019 at 00:07, nadir view (a),(b); Sentinel-3B/SLSTR image collected on Raikoke the 22 June 2019 at 23:01, nadir view (c),(d). (a),(c): red pixels display the manual plume mask (MPM) obtained from the analysis on the specific image; (b),(d): comparison between volcanic ash detected by NN and MPM; green pixels indicate the areas for which both NN and MPM detect ashy pixels, red pixels indicate the areas for which only MPM detects ashy pixels, blue pixels indicate the areas for which only NN detects ashy pixels.

263 Besides the NN plume mask validation, we also compared the pixels which the NN model classified as affected by weather

264 clouds (hereafter NNCM) with the SLSTR standard product for meteorological clouds.
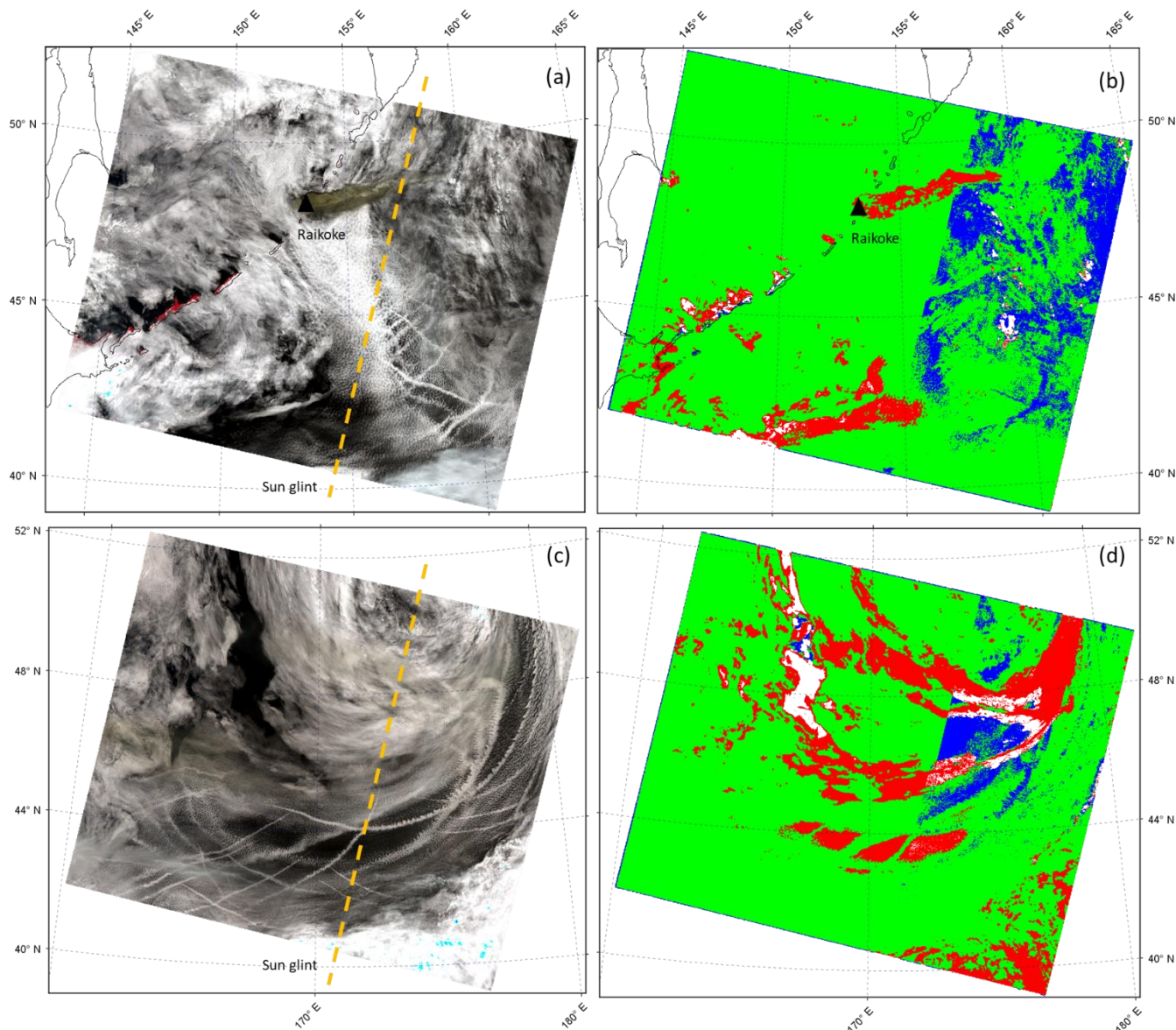
Figure 9: Sentinel-3A/SLSTR image collected on Raikoke the 22 June 2019 at 00:07, nadir view (a),(b); Sentinel-3B/SLSTR image collected on Raikoke the 22 June 2019 at 23:01, nadir view (c),(d). (a),(c): RGB view; (b),(d): comparison between cloud mask retrieved by NN and standard Sentinel-3 confidence in summary cloud mask (CSCM); green pixels indicate the areas for which both NN and CSCM detect cloudy pixels, red pixels indicate the areas for which only CSCM detects cloudy pixels, blue pixels indicate the areas for which only NN detects cloudy pixels.

271 Among the cloud masks available in the SLSTR L1RBT product, the *confidence_in_summary_cloud* mask (hereafter CSCM)

272 is considered. The CSCM is a cloud mask which discriminates cloud pixels (*true*) and cloud-free pixels (*false*); it is an ultimate

273 cloud mask product derived from several separated cloud tests (Sentinel-3-SLSTR-Land-Handbook, 2021). Because of the

274 CSCM doesn't distinguish between meteo clouds and meteo ice clouds as the NN algorithm does, the comparison is realized

275 by considering the whole NN meteo cloud classes (i.e. the sum between *Cloud* and *Cloud_ice*).

276 Figure 9 displays the RGB composite, in which the Sentinel-3 sun glint mask is highlighted (right part of the scene), and the

277 comparison between NN cloud mask and S3 cloud mask for S3A/SLSTR image collected on Raikoke the 22 June 2019 at

278 00:07 UTC (Figure 9(a) and Figure 9(b)) and for S3B/SLSTR image collected on Raikoke the 22 June 2019 at 23:01 UTC

279 (Figure 9(c) and Figure 9(d)).

280 Also in this case, for the images displaying the comparison between the two types of cloud masks (Figure 9(b) and Figure

281 9(d)), green indicates the pixels classified as cloud for both procedures, while red and blue indicate the pixels classified as

282 cloud only from the SLSTR standard product and NN, respectively. Pixels that are not coloured are associated to a cloud-free

283 condition for both the NN and the S3 cloud mask. Looking at the comparison, a very good agreement between the NN meteo

284 cloud mask and the SLSTR standard cloud mask can be observed, with high amount of pixels classified as affected by clouds

285 by both products (see Table 5). Moreover, looking at the red pixels in the 23:01 UTC image especially, it can be noted that the

286 SLSTR cloud mask includes also the volcanic cloud.

287

288 **Table 5:** Comparison between the NN cloud mask (NNCM) and the confidence in summary cloud mask (CSCM) for each SLSTR classified
289 product (pixels number for each class). The total number of classified pixels is 1614405 for the S3A/SLSTR at 00.07 UTC image and
290 1701319 for the S3B/SLSTR at 23.01 UTC image respectively.

Product Classified Product	NNCM and CSCM	Only NNCM	Only CSCM
S3A/SLSTR at 00.07 UTC	1332632	163225	91768
S3B/SLSTR at 23.01 UTC	1291989	65359	284193

291

292 From the validation procedure we have carried out, a considerable point which has to be underlined is that, unlike adopting a

293 time consuming and case-specific approach as MPM which also needs a manual operation by setting various thresholds for

294 each case under examination, the NN model can be used to discriminate ash plume in satellite images with good accuracy in

295 a fast and automatic way.

296

297 **5 Conclusions**

298 In this work the results of a new neural network based approach for volcanic cloud detection are described. The algorithm,

299 developed to process Sentinel-3/SLSTR daytime images, exploits the use of MODIS daytime data as training. The procedure

300 allows the full characterization of the SLSTR image by identifying, besides the volcanic cloud, the surfaces under the cloud

301 itself, the meteorological clouds (and phases), land and sea surfaces. As test cases, the S3A-S3B/SLSTR images collected over

302 the Raikoke volcano area during the June 2019 eruption have been considered.

The proposed neural network based approach for volcanic ash detection and image classification shows an overall good accuracy for the ash class, which is the main target of the algorithm, and for the meteorological cloud class also. A strong effectiveness of the NN classification is indeed also related to the cloudy pixel recognition, with the ability to distinguish two different types of meteorological clouds composed of water droplets and ice respectively. It has to be reminded that the wide distribution of meteorological clouds in the scenario under consideration makes the ash detection task particularly complex, since weather ice clouds and volcanic clouds exhibit similar spectral behaviour.

A point to be underlined is the valuable advantage of the developed procedure related to the creation of products (the eight classes) not all already available as SLSTR standard products; this fact represents a considerable step forward for generation of novel type of S3/SLSTR products.

A post processing has been applied to NN outputs by exploiting the land/sea mask of SLSTR standard products, in order to mitigate the insurgence of NN land/sea failure, being the land/sea mask always available as SLSTR standard product.

The comparison between the NN plume mask and a reference plume mask (MPM) taken as *ground truth*, shows a good agreement between the two techniques. The significant result lies in the fact that the overall good performance of the NN output is achieved in an automatic way and with a brief processing time, compared to the plume mask generated ad hoc, which instead requires longer time, is case-specific and it needs the presence of an operator. The other considerable achievement of the NN developed procedure indeed is that, once the NN model has been properly trained, it has been used to detect the ash plume for each SLSTR image related to the Raikoke eruption, while the creation of the MPM has to be made separately for each image.

The comparison between the NN cloud mask and the cloud mask derived from SLSTR standard products has been also carried out, resulting in high percentage of agreement between the two products.

A promisingly outcome is related to the ability of the NN model to generalize over different data in terms of spatiotemporal and geographical characteristics, being the NN model trained with data collected over the Iceland region in 2010 and then applied to data acquired over the Kamchatka Peninsula in Russia in 2019. One of the point under consideration for future improvements is to enhance the ability of the NN to generalize over various eruptive scenarios, by integrating different training dataset (in terms of regions, type of eruption, time interval, etc). We also aim at further investigating some aspects in order to improve the classification accuracy, as the introduction of other output classes, such as volcanic ice cloud, and the integration of other variables in the model, such as the sensor view angle. Finally, the possibility to use S3/SLSTR products as training dataset instead of using MODIS data is an essential point to be taken into account in order to increase the accuracy of the algorithm.

Data availability

Terra-Aqua/MODIS data are distributed from the Level-1 and Atmosphere Archive & Distribution System (LAADS) Distributed Active Archive Center (DAAC) and they are available at: https://ladsweb.modaps.eosdis.nasa.gov/search/.

335 Sentinel-3/SLSTR data are distributed from the Copernicus Open Access Hub and they are available at:
336 https://scihub.copernicus.eu/dhus/#/home.

337 **Author contributions**

338 IP and DDS developed algorithms, analyzed data and results and wrote the manuscript; MP developed algorithms and
339 methodology, analyzed data and results and reviewed the manuscript; SC and LG analyzed data and results, provided reference
340 data for validation task and wrote-reviewed the manuscript; FP supported the analysis of data and results, worked on the
341 Himawari-8 analysis and on the relative part of the manuscript, and reviewed the manuscript; LM and DS supported the
342 analysis of data and results; FDF reviewed the manuscript, supervised the research and contributed to funding acquisition;
343 GSal supported the analysis of data and results and worked on validation; GSch supports the research and contributed to
344 funding acquisition.
345 All authors have read and agreed to the published version of the manuscript.

346 **Competing interests**

347 The authors declare that they have no conflict of interest.

348 **Disclaimer**

349 Publisher's note: Copernicus Publications remains neutral with regard to jurisdictional claims in published maps and
350 institutional affiliations.

351 **Special issue statement**

352 This article is part of the special issue "Satellite observations, in situ measurements and model simulations of the 2019 Raikoke
353 eruption (ACP/AMT/GMD inter-journal SI)". It is not associated with a conference.

354 **Acknowledgments**

355 The results shown in this work were obtained in the framework of the VISTA (Volcanic monItoring using SenTinel sensors
356 by an integrated Approach) project, which was funded by ESA within the "EO Science for Society framework"
357 [https://eo4society.esa.int/projects/vista/].

Financial support

Not applicable.

References

Atkinson, P. M., and Tatnall, A. R.: Introduction Neural networks in remote sensing, International Journal of Remote Sensing, 18(4), 699-709, https://doi.org/10.1080/014311697218700, 1997.

Bishop, C.M., 1994. Neural networks and their applications. Review of Scientific Instruments, 65 (6), pp. 1803-1832.

Bourassa, A.E.; Robock, A.; Randel, W.J.; Deshler, T.; Rieger, L.A.; Lloyd, N.D.; Llewellyn, E.J.; Degenstein, D.A. Large Volcanic Aerosol Load in the Stratosphere Linked to Asian Monsoon Transport. Science 2012, 337, 78–81, doi:10.1126/science.1219371.

Casadevall, T.J. The 1989/1990 eruption of Redoubt Volcano Alaska: Impacts on aircraft operations. J. Volcanol. Geotherm. Res. 1994, 62, 301–316

Corradini S., Spinetti C., Carboni E., Tirelli C., Buongiorno M. F., Pugnaghi S. and Gangale G.: "Mt. Etna tropospheric ash retrieval and sensitivity analysis using moderate resolution imaging spectroradiometer measurements," Journal of Applied Remote Sensing 2(1), 023550 (1 November 2008). https://doi.org/10.1117/1.3046674.

Corradini, S.; Merucci, L.; Prata A.J. Retrieval of SO2 from thermal infrared satellite measurements: Correction procedures for the effects of volcanic ash. Atmos. Meas. Tech. 2009, 2, 177–191.

Craig, H.; Wilson, T.; Stewart, C.; Outes, V.; Villarosa, G.; Baxter, P. Impacts to agriculture and critical infrastructure in Argentina after ashfall from the 2011 eruption of the Cordón Caulle volcanic complex: an assessment of published damage and function thresholds. J. Appl. Volcanol. 2016, 5, 7, doi:10.1186/s13617-016-0046-1.

Delmelle, P.; Stix, J.; Baxter, P.; Garcia-Alvarez, J.; Barquero, J. Atmospheric dispersion, environmental effects and potential health hazard associated with the low altitude gas plume of Masaya volcano, Nicaragua. Bull. Volcanol. 2002, 64, 423–434.

Di Noia A., Sellitto P, Del Frate F, de Laat J., Global tropospheric ozone column retrievals from OMI data by means of neural networks, Atmospheric Measurement Techniques, 6, 895–915, 2013.

381 Di Noia, A. and Hasekamp, O. P. (2018). Neural networks and support vector machines and their application to aerosol and
382 cloud remote sensing: a review. Springer Series in Light Scattering, 279-329.

383 Francis P. N., Cooke M. C., and Saunders R. W., Retrieval of physical properties of volcanic ash using Meteosat: A case study
384 from the 2010 Eyjafjallajokull eruption. J. Geophys. Res., 117:D00U09, 2012. doi: 10.1029/2011JD016788.

385 Gardner, M. W., & Dorling, S. R., 1998. Artificial neural networks (the multilayer perceptron) – a review of applications in
386 the atmosphere sciences. Atmospheric Environment, 32(14-15), 2627-2636.

387 Haywood, J.; Boucher, O. Estimates of the direct and indirect radiative forcing due to tropospheric aerosols: a review. Rev.
388 Geophys. 2000, 38, 513–543. Robock, A. Volcanic eruptions and climate, Rev. Geophys. 2000, 38, 191–219.

389 Horwell, C.J.; Baxter, P.J. The respiratory health hazards of volcanic ash: A review for volcanic risk mitigation. Bull. Volcanol.
390 2006, 69, 1–24.

391 Horwell, C.J.; Baxter, P.J.; Hillman, S.E.; Calkins, J.A.; Damby, D.E.; Delmelle, P.; Donaldson, K.; Dunster, C.; Fubini, B.;
392 Kelly, F.J.; et al. Physicochemical and toxicological profiling of ash from the 2010 and 2011 eruptions of Eyjafjallajökull and
393 Grímsvötn volcanoes, Iceland using a rapid respiratory hazard assessment protocol. Environ. Res. 2013, 127, 63–73.

394 Mather, T.A.; Pyle, D.M.; Oppenheimer, C. Tropospheric volcanic aerosol. Geophysical Monograph 2003, 139, 189–212.

395 Oppenheimer, C.; Scaillet, B.; Martin, S. Sulfur degassing from volcanoes: source conditions, surveillance, plume chemistry
396 and Earth system impacts. Reviews in Mineralogy and Geochemistry 2011, 73, 363–421, doi:10.2138/rmg.2011.73.13.

397 Pavolonis M. J., "Advances in Extracting Cloud Composition Information from Spaceborne Infrared Radiances. A Robust
398 Alternative to Brightness Temperatures", Part I: Theory. J. Appl. Meteor. Climatol., 49:1992-2012, 2010. doi:
399 10.1175/2010JAMC2433.1.

400 Pavolonis M. J. and Sieglaff J., "GOES-R Advanced Baseline Imager (ABI) Algorithm Theoretical Basis Document For
401 Volcanic Ash (Detection and Height). Technical report", NOAA NESDIS STAR, 2010.

402 http://cimss.ssec.wisc.edu/~mpav/GOESR_ABI_ATBD_Aviation_VolAsh_v2.1.pdf.

403 Picchiani, M., Chini, M., Corradini, S., Merucci, L., Sellitto, P., Del Frate, F., and Stramondo, S.: Volcanic ash detection and
404 retrievals using MODIS data by means of neural networks, Atmos. Meas. Tech., 4, 2619–2631, https://doi.org/10.5194/amt 4-
405 2619-2011, 2011.

406 Picchiani, M., Chini, M., Corradini, S., Merucci, L., Piscini, A. and Del Frate, F., 2014. Neural network multispectral satellite
407 images classification of volcanic ash plumes in a cloudy scenario. Annals of Geophysics, Special Issue on "Atmospheric
408 Emissions from Volcanoes", Vol. 57, Fast Track 2. doi: 10.4401/ag-6638.

409 Picchiani M., Del Frate F. and Sist M., "A Neural Network Sea-Ice Cloud Classification Algorithm for Copernicus Sentinel-3
410 Sea and Land Surface Temperature Radiometer," IGARSS 2018 - 2018 IEEE International Geoscience and Remote Sensing
411 Symposium, Valencia, Spain, 2018, pp. 3015-3018, doi: 10.1109/IGARSS.2018.8517857.

412 Piscini, A., Picchiani, M., Chini, M., Corradini, S., Merucci, L., Del Frate, F., and Stramondo, S., 2014. A Neural Network
413 approach for the simultaneous retrieval of volcanic ash parameters and SO2 using MODIS data", AMT, 7, 4023-4047.
414 doi:10.5194/amt-7-4023-2014.

415 Prata A. J., (1989a) Observations of volcanic ash clouds in the 10-12 μm window using AVHRR/2 data, International Journal
416 of Remote Sensing, 10: 4-5, 751-761, DOI: 10.1080/01431168908903916.

417 Prata A. J., (1989b) Infrared radiative transfer calculations for volcanic ash clouds, «Geophysical Research Letters»,Vol. 16.

418 Prata, A. J., Bluth, G., Rose, B., Schneider, D., Tupper, A., "Comments on ''Failures in detecting volcanic ash from a satellite-
419 based technique''", Remote Sensing of Environment 78 (2001a) 341– 346.

420 Prata A. J. and Grant I. F., "Determination of mass loadings and plume heights of volcanic ash clouds from satellite data,"
421 CSIRO Atmosph. Res. Tech. Pap. 48, 39, Commonw. Sci. and Ind. res. Organ., Melbourne, Victoria, Australia (2001b).

422 Sellitto P., Del Frate F., Solimini D., Casadio S., "Tropospheric ozone column retrieval from ESA-Envisat SCIAMACHY
423 nadir UV/VIS radiance measurements by means of a neural network algorithm," IEEE Transactions on Geos. and Rem. Sens.,
424 vol. 50, n. 3, pp. 998-1011, March 2012.

425 Sentinel-3-SLSTR-Land-Handbook: https://sentinel.esa.int/documents/247904/4598082/Sentinel-3-SLSTR-Land-
426 Handbook.pdf/, last access: January 2022, 2021.

427 Shinohara, H. Excess degassing from volcanoes and its role on eruptive and intrusive activity. Rev. Geophys. 2008, 46,
428 RG4005, doi:10.1029/2007RG000244.

429 Solomon, S.; Daniel, J.S.; Neely, R.R.; Vernier, J.P.; Dutton, E.G.; Thomason, L.W. The persistently Variable "Background"
430 Stratospheric Aerosol Layer and Global Climate Change. Science 2011, 333, 866–870, doi:10.1126/science.1206027.

431   Zehner, C. Monitoring volcanic ash from space. In Proceedings of the ESA-EUMETSAT Workshop on the 14 April to 23 May

432   2010 Eruption at the Eyjafjoll Volcano, South Iceland, Frascati, Italy, 26–27 May 2010.